JNS PEDIATRICS

CLINICAL ARTICLE

Fully automated, real-time, calibration-free, continuous noninvasive estimation of intracranial pressure in children

Andrea Fanelli, PhD,[1] Frederick W. Vonberg, MBBS,[1,2] Kerri L. LaRovere, MD,[3] Brian K. Walsh, PhD,[2] Edward R. Smith, MD,[4] Shenandoah Robinson, MD,[4,5] Robert C. Tasker, MBBS, MD,[2,3] and Thomas Heldt, PhD[1]

[1]Institute for Medical Engineering and Science, Massachusetts Institute of Technology, Cambridge; [2]Department of Anesthesiology, Critical Care and Pain Medicine, and Departments of [3]Neurology and [4]Neurosurgery, Boston Children's Hospital, Boston, Massachusetts; and [5]Department of Neurosurgery, Johns Hopkins University, Baltimore, Maryland

OBJECTIVE In the search for a reliable, cooperation-independent, noninvasive alternative to invasive intracranial pressure (ICP) monitoring in children, various approaches have been proposed, but at the present time none are capable of providing fully automated, real-time, calibration-free, continuous and accurate ICP estimates. The authors investigated the feasibility and validity of simultaneously monitored arterial blood pressure (ABP) and middle cerebral artery (MCA) cerebral blood flow velocity (CBFV) waveforms to derive noninvasive ICP (nICP) estimates.

METHODS Invasive ICP and ABP recordings were collected from 12 pediatric and young adult patients (aged 2–25 years) undergoing such monitoring as part of routine clinical care. Additionally, simultaneous transcranial Doppler (TCD) ultrasonography–based MCA CBFV waveform measurements were performed at the bedside in dedicated data collection sessions. The ABP and MCA CBFV waveforms were analyzed in the context of a mathematical model, linking them to the cerebral vasculature's biophysical properties and ICP. The authors developed and automated a waveform preprocessing, signal-quality evaluation, and waveform-synchronization "pipeline" in order to test and objectively validate the algorithm's performance. To generate one nICP estimate, 60 beats of ABP and MCA CBFV waveform data were analyzed. Moving the 60-beat data window forward by one beat at a time (overlapping data windows) resulted in 39,480 ICP-to-nICP comparisons across a total of 44 data-collection sessions (studies). Moving the 60-beat data window forward by 60 beats at a time (nonoverlapping data windows) resulted in 722 paired ICP-to-nICP comparisons.

RESULTS Greater than 80% of all nICP estimates fell within ± 7 mm Hg of the reference measurement. Overall performance in the nonoverlapping data window approach gave a mean error (bias) of 1.0 mm Hg, standard deviation of the error (precision) of 5.1 mm Hg, and root-mean-square error of 5.2 mm Hg. The associated mean and median absolute errors were 4.2 mm Hg and 3.3 mm Hg, respectively. These results were contingent on ensuring adequate ABP and CBFV signal quality and required accurate hydrostatic pressure correction of the measured ABP waveform in relation to the elevation of the external auditory meatus. Notably, the procedure had no failed attempts at data collection, and all patients had adequate TCD data from at least one hemisphere. Last, an analysis of using study-by-study averaged nICP estimates to detect a measured ICP > 15 mm Hg resulted in an area under the receiver operating characteristic curve of 0.83, with a sensitivity of 71% and specificity of 86% for a detection threshold of nICP = 15 mm Hg.

CONCLUSIONS This nICP estimation algorithm, based on ABP and bedside TCD CBFV waveform measurements, performs in a manner comparable to invasive ICP monitoring. These findings open the possibility for rational, point-of-care treatment decisions in pediatric patients with suspected raised ICP undergoing intensive care.

https://thejns.org/doi/abs/10.3171/2019.5.PEDS19178

KEYWORDS intracranial pressure; traumatic brain injury; patient monitoring; mathematical modeling; multimodality data analytics; trauma

ABBREVIATIONS ABP = arterial blood pressure; AUC = area under the ROC curve; *C* = compliance; CBFV = cerebral blood flow velocity; *g* = gravitational acceleration; GCS = Glasgow Coma Scale; h = vertical height difference between invasive ABP and ICP transducer locations; ICP = intracranial pressure; MAE = mean absolute error; MedAE = median absolute error; MCA = middle cerebral artery; nICP = noninvasive ICP; *R* = resistance; RMSE = root-mean-square error; ROC = receiver operating characteristic; SDE = standard deviation of the error; SQA = signal quality assessment; TBI = traumatic brain injury; TCD = transcranial Doppler; ρ = density of blood.

SUBMITTED April 3, 2019. **ACCEPTED** May 28, 2019.
INCLUDE WHEN CITING Published online August 23, 2019; DOI: 10.3171/2019.5.PEDS19178.

Invasive intracranial pressure (ICP) monitoring is used to direct medical interventions that target the development and consequences of elevated intracranial pressure (ICP) related to severe traumatic brain injury (TBI) and other etiologies such as late sequelae of craniosynostosis, metabolic disorders, and selected causes of encephalopathy.[10,11] However, significant regional variation exists in the use of invasive ICP monitoring. In children with moderate TBI, management often occurs without the benefit of ICP monitoring.[2,3] Historically, various initial ICP target values have been used to guide treatment, from less than 15 mm Hg, to less than 20 mm Hg, or even less than 25 mm Hg.[10] Use of cerebral perfusion pressure to guide care also requires knowledge of ICP. Recently, it has been suggested that noninvasive ultrasound measurement of the optic nerve sheath diameter may be used to identify and monitor elevated ICP. However, such measurements are neither suitable for continuous real-time monitoring nor are they able to provide absolute ICP.[16]

In this report, we present a fully automated biomedical modeling and signal processing approach to estimate ICP that has applicability in neurosurgical practice. ICP is estimated noninvasively from transcranial Doppler (TCD) ultrasound measurements of the middle cerebral artery (MCA) cerebral blood flow velocity (CBFV) and invasive radial arterial blood pressure (ABP). CBFV measurements are routinely performed in most tertiary pediatric hospitals that typically care for children with neurological diseases who might require ICP monitoring. Here, we first demonstrate the feasibility of automated signal-quality evaluation, waveform synchronization, and noninvasive ICP (nICP) estimation. Then, by evaluating the accuracy and precision in 12 pediatric patients undergoing invasive ICP monitoring, we demonstrate that the model-based algorithm for real-time, continuous, and noninvasive ICP estimation performs in a manner comparable to invasive monitoring in children. Importantly, this technique does not require comparison to a standardized population norm, which makes it particularly suitable for complex children who would benefit from patient-specific ICP monitoring.

Methods

ICP Estimation

To estimate ICP, we used a previously developed mechanistic model that links simultaneously acquired ABP and CBFV waveform measurements to ICP and the biophysical properties of the cerebrospinal and cerebrovascular systems (Fig. 1A).[9] The biophysical properties of a major cerebrovascular territory and surrounding brain tissue are represented by a single compliance and a single resistive element. The compliance element *C* captures the aggregate elastic properties of the MCA and surrounding brain tissue. The resistance element *R* represents the aggregate cerebrovascular resistance to blood flow through the vascular territory. The model imposes a mathematical constraint on the relationship between the input waveforms (ABP and CBFV) on the one hand, and the model parameters (*R*, *C*, and ICP) on the other (see Supplementary Material for details).[9] We defined an "estimation window" as 60 consecutive beats of ABP and CBFV waveform data and leveraged the constraint implied by the model in Fig. 1A to produce one estimate of *R*, *C*, and ICP for each 60-beat estimation window.

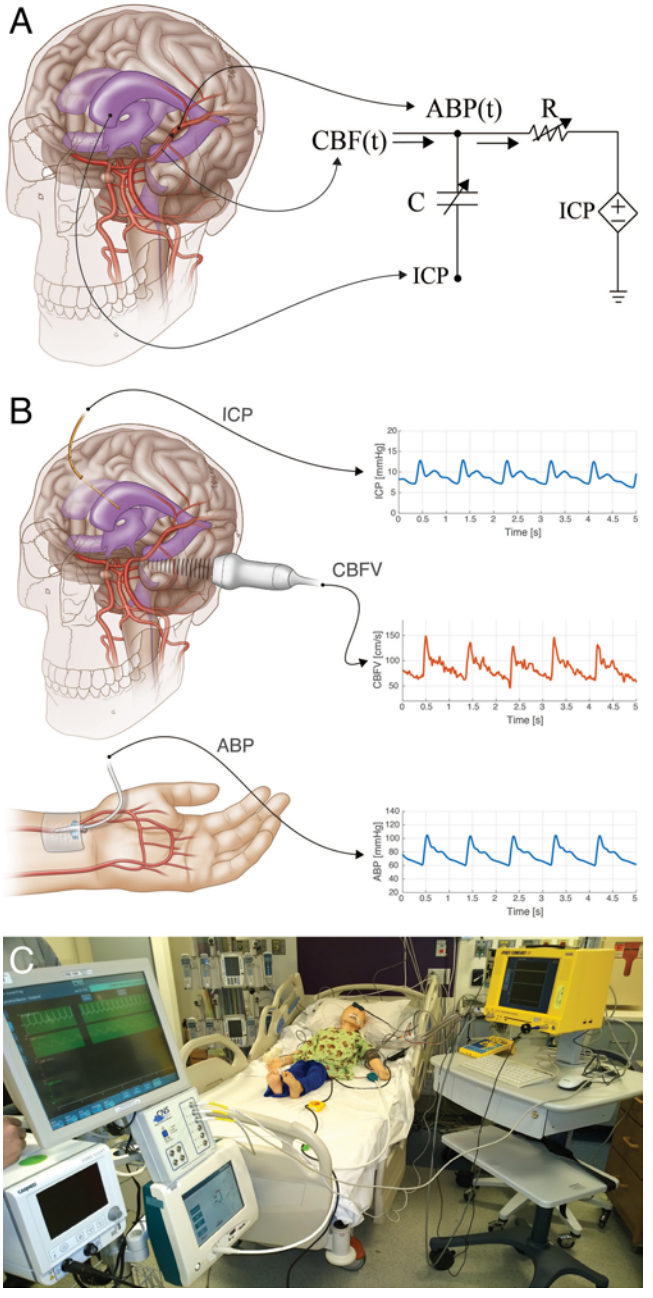

FIG. 1. A: Model-based representation of cerebrovascular physiology for nICP estimation. **B:** Available bedside measurements in intensive care. **C:** Simulated data-acquisition setup used in the critical care setting at Boston Children's Hospital. Anatomical drawings in panels A and B, copyright Sara Jarret, CMI, Atlas InMedia. Published with permission.

Clinical Study Protocol and Data Collection

Our study protocol was approved by the institutional review boards at Boston Children's Hospital and the Mas-

sachusetts Institute of Technology. Informed consent and assent (when appropriate) were obtained from the patient or their legally authorized representatives. Clinical data collection occurred in the medical and surgical intensive care unit at Boston Children's Hospital from February 2015 to June 2017.

Data collection occurred up to twice daily during dedicated bedside recording sessions for the duration that invasive ICP and ABP monitoring were indicated for clinical management. Both waveforms were recorded by MP-90 bedside monitors (Philips Healthcare). The ICP transducers were referenced to the level of the tragus, while the ABP transducers were referenced to the level of the heart. Right and left MCA CBFV waveform recordings were performed using the ST3 TCD ultrasound system (Spencer Technologies) and conducted by members of the study team experienced and credentialed in TCD ultrasonography (K.L.L.) or those having undergone proctored hands-on TCD training sessions (F.W.V., B.K.W.). The simultaneously acquired ABP, ICP, and CBFV waveforms were streamed digitally, nominally at 125 samples/sec, to a Moberg Component Neuromonitoring System (Moberg Research) for archiving (Fig. 1C). During each data acquisition session, we also recorded the patient's most recent Glasgow Coma Scale (GCS) score and the most recent hematocrit value. Additionally, we performed bedside measurements of the vertical height of the pressure transducers. For each patient, we also recorded demographic data (patient age, sex, race, and ethnicity) and clinical information (etiology of encephalopathy, anatomical location of injury if focal rather than generalized, and type and location of invasive ICP sensor). Recordings were deidentified, and nICP estimation was performed in a manner blinded to the measured ICP.

Signal Processing Pipeline

Our estimation approach relies on a model-based analysis of synchronized ABP and MCA CBFV waveform measurements. The quality of the nICP estimates critically depends on 2 aspects of the collected ABP and CBFV waveforms: their signal quality and the time alignment between the 2 waveforms. To achieve robust and reliable nICP estimation, we developed a fully automated signal preprocessing pipeline consisting of 5 major steps (described in detail below): 1) coarse signal quality assessment (SQA), 2) data batch selection, 3) fine SQA on selected data batches, 4) final data segment selection for nICP estimation (Fig. 2), and 5) waveform synchronization and beat-onset alignment.

Step 1: Coarse Signal Quality Assessment

During coarse SQA, the algorithm identifies regions of the ABP and CBFV signals with nonphysiological amplitudes (Fig. 2A and D). For the ABP waveform, we performed beat-onset detection and identified any beat containing a sample with an amplitude value above 300 mm Hg or below 20 mm Hg.[23] Additionally, we identified any beat with a pulse pressure less than 20 mm Hg. For the CBFV waveform, we identified any beat containing a sample value above 300 cm/sec or less than 20 cm/sec. To prevent the rejection of long stretches of data on the basis of brief artifacts or short noisy segments, we only rejected flagged regions of data longer than 3 seconds in duration.

Step 2: Data Batch Selection

Based on pilot analyses, a priori we defined a data batch as a continuous period of 30 beats or longer over which ABP or CBFV sample values contained less than 3 seconds of data rejected by coarse SQA filtering (Fig. 2B and E).

Step 3: Fine Signal Quality Assessment

Following the identification of selected data batches, the algorithm performed more detailed SQA by evaluating morphological characteristics of the ABP and CBFV waveforms (see Supplementary Material for details).[6,21] Briefly, we evaluated the beat-by-beat ABP waveform quality by first computing, for each beat, the mean absolute sample-by-sample difference. We then normalized the resultant difference metric for each individual beat by a running average of the past mean absolute differences. This metric assumes large values in regions in which the waveform morphology is corrupted by noise and artifact. The beat-by-beat CBFV signal quality was determined by first computing the spectral correlation between the ABP and CBFV signals over a sliding window of 8 seconds in duration and then quantifying the deviation of each CBFV wavelet from an adaptively updated wavelet template (see Supplementary Material).[21] CBFV wavelets with large normalized mean-square errors in comparison with the template waveform were flagged for rejection. In a final postprocessing step, regions of the input data were deemed unacceptable if either the ABP wavelet or the corresponding CBFV wavelet had been flagged for rejection by fine SQA filtering (Supplemental Figure S1).

Step 4: Data Segment Selection

We defined data segments as continuous stretches of input data that were retained after coarse and fine SQA (Fig. 2C and F).

Step 5: Waveform Synchronization and Beat Alignment

In order to achieve fully automated, calibration-free nICP estimation, we required synchronization and beat alignment of the ABP, ICP, and CBFV waveforms for 3 main reasons. First, since the ABP and CBFV waveforms are acquired by different bedside devices with unsynchronized internal clocks and streamed digitally to our data acquisition system, slight deviations in clock frequencies from their respective nominal, manufacturer-specified values lead, cumulatively over time, to significant drift (de-synchronization) between the two waveforms (Fig. 3A–C). Second, each monitoring device performs its own internal signal processing steps that lead to an unknown delay between the time a physiological change registers at the device's sensor and the corresponding appearance of the measured change in the device's output channel. Third, our nICP estimation algorithm assumes ABP measured at the MCA, rather than ABP measured peripherally. Since MCA ABP waveform measurements are not available, we needed to shift the measured ABP waveform from the radial artery in time relative to the MCA CBFV

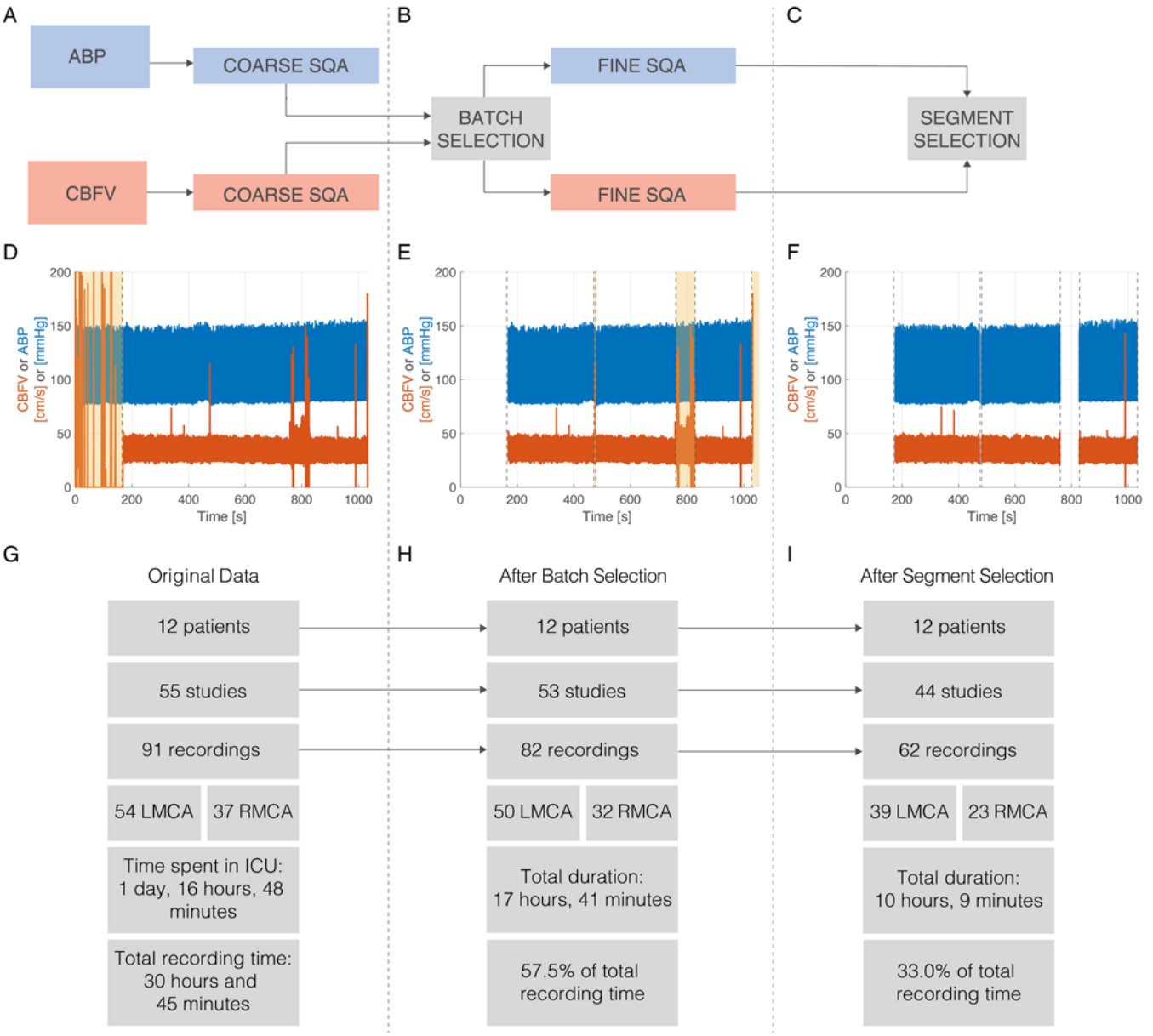

FIG. 2. A and D: Coarse SQA for rejection of unphysiological data regions. **B and E:** Batch selection and fine SQA for rejection of individual ABP and CBFV beats of insufficient waveform quality. **C and F:** Final data segment selection for ICP estimation after coarse and fine SQA. **G–I:** Associated bedside data recording statistics before (G) and after (H) coarse and fine (I) SQA.

waveform, such that their phase relationship approximates that between the MCA ABP and CBFV.

To correct the waveform drift introduced by the (unknown but inevitable) deviations of the clock speeds of the Philips bedside monitor and the Spencer TCD system from their respective nominal values, we first aligned the waveform samples by sample number. The time stamp for each sample was then renormalized based on a common nominal sampling frequency of 125 samples/sec. We then determined the beat-onset series $n(i)$ and $m(i)$ for ABP and CBFV, respectively; and computed the resulting beat-by-beat phase lag $\tau_i = m(i) - n(i)$ between the two waveforms as a function of renormalized time (Fig. 3A and B). Plotting the phase lag series τ_i against renormalized time demonstrates the linear nature of the phase drift (Fig. 3C), which is indicative of 2 stable clocks that operate at slightly different frequencies. Our automated pipeline compensates for this linear waveform desynchronization by fitting a first-order (linear) regression model ($\hat{\tau}(t) = \alpha \times t + \beta$) in a least-squares manner. We adjusted the time vector for the CBFV samples according to $t_{new} = t(1 - \hat{\alpha})$, where $\hat{\alpha}$ is the least-squares estimate of the slope parameter α from the linear regression analysis. The resultant time series [t, ABP] of the collected ABP waveform and the adjusted CBFV time series [t_{new}, CBFV] are thus synchronized along a shared, common time axis with zero-mean phase

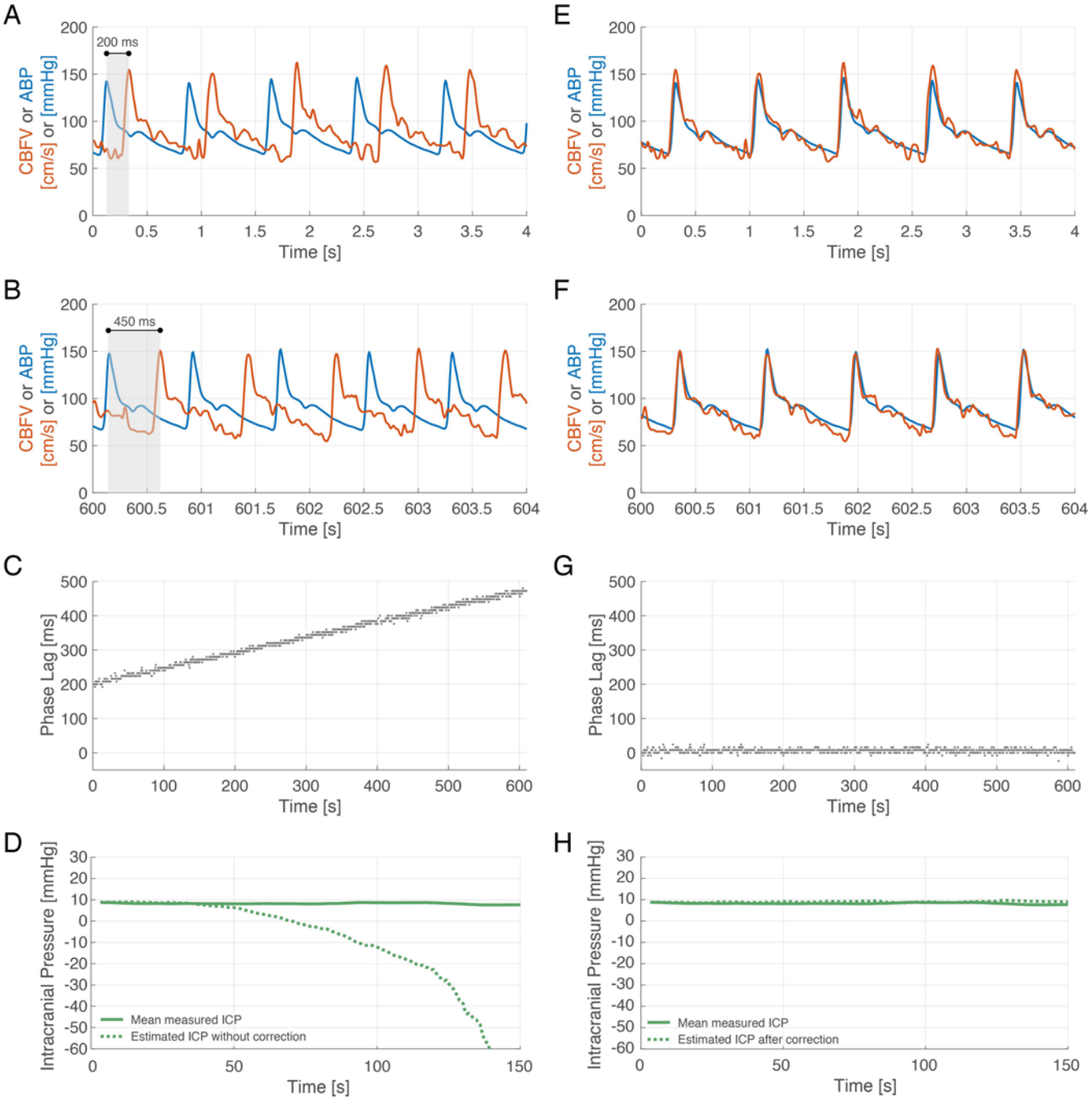

FIG. 3. A: Phase relationship between ABP and CBFV waveforms at the beginning of the recording session. **B:** After 10 minutes of recording, the phase difference has increased significantly due to the inevitable timing differences between the clocks of the ABP monitor and TCD system. **C:** The phase lag increases linearly with recording duration. **D:** ICP estimation without ABP and CBFV waveform synchronization, resulting in complete failure of ICP estimation within 40 seconds. **E–G:** Phase relationship between ABP and CBFV waveforms after waveform synchronization and beat-onset alignment (E and F) indicating zero-mean phase drift over time (G). **H:** ICP estimation and measured mean ICP after post hoc waveform synchronization and beat-onset alignment.

drift (Fig. 3E–G), although corresponding beats might not necessarily be aligned.

In order to quantify and compensate for a possible delay between the registered waveforms, the preprocessing pipeline estimates the shift required to align the onsets of corresponding beats of the ABP and CBFV waveforms. The required shift is determined as the time lag of the dominant peak of the cross-correlation between the two waveforms (Supplemental Figure S2). The delay is computed once for each recording session and subtracted from the CBFV time stamps to beat-align the CBFV and ABP waveform signals.

Mean ABP Correction

Our model assumes ABP measurements referenced to the level of the MCA. We therefore performed a hydrostatic pressure correction of the ABP waveform to compensate for the fact that the measured ABP was referenced to the level of the heart, rather than the MCA. We estimated the difference in mean pressure by determining the hydrostatic pressure ($\rho \times g \times h$) of a theoretical column of blood between the two transducer locations. We estimated the blood density (ρ) on the basis of the patient's most recent hematocrit measurement and the regression analysis by Hinghofer-Szalkay et al.[8] We also evaluated the magnitude of the effect of using patient-specific hematocrit measurements on the nICP estimates versus an assumed value for the blood density of 1.06 g/ml. We determined "h" during every recording session by measuring the difference between the vertical heights of the ABP and ICP transducer locations. Finally, we subtracted the estimated hydrostatic pressure offset from the measured ABP waveform to arrive at our estimated MCA ABP waveform. Next, we applied a bandpass filter with cutoff frequencies at 0.5 and 12 Hz to the ABP and CBFV waveforms before proceeding to nICP estimation.

Statistical Analysis

We quantified the performance of our nICP estimation by computing the mean error (bias or accuracy) between the nICP and the mean of the invasively measured ICP waveform for corresponding 60-beat data windows. We also calculated the associated standard deviation of the error (SDE or precision), and computed the root-mean-square error (RMSE) between nICP estimates and ICP measurements as an aggregate measure of estimation performance.[20]

In one analysis approach, the estimation results were computed for sliding (overlapping) data windows in which the 60-beat estimation window was advanced one beat at a time to give beat-by-beat nICP estimates. In an alternative approach, the nICP estimates were computed on hopping (nonoverlapping) estimation windows in which the data windows were advanced by a full frame of 60 beats. The hopping-window estimation approach results in one nICP update every half to full minute, depending on the patient's mean heart rate. We also averaged the window-by-window nICP estimates for each recording session and for each patient to obtain the per-session and per-patient bias, SDE, and RMSE.

We quantified the performance of detecting elevated ICP by computing the sensitivity and specificity of detecting a mean measured ICP value above 15 mm Hg (approximately 20 cm H_2O) on the basis of nICP > 15 mm Hg. By sweeping the nICP threshold from 0 to 30 mm Hg, we obtained the full receiver operating characteristic (ROC) and determined the area under the ROC curve (AUC). Differences in the distributions of the estimation errors were tested for statistical significance using the Wilcoxon rank-sum test with the significance level set to 0.05.[20]

Data Availability

The data collected in this study will be made available through PhysioNet (physionet.org), not least because there has been much interest in nICP estimation over the past 2 decades.[4]

Results

Patient Cohort

The study cohort comprised 12 patients (9 males and 3 females), with a median age of 11 years (IQR 6.5–17.0 years), median GCS score 7 (IQR 3–13), and a variety of pathologies necessitating invasive ICP monitoring (cerebrovascular disorder, 4; brain mass or neurosurgical problem, 4; severe TBI, 3; metabolic abnormality, 1). We succeeded in acquiring unilateral CBFV recordings in all patients. We were unable to obtain bilateral recordings in 3 patients because of recent surgery, lack of scalp integrity, or problems that limited placement of the TCD probe in the temporal region. The mean measured ICP in our study cohort ranged from 1.4 to 23.9 mm Hg (IQR 8.0–13.4 mm Hg).

Signal-Quality Assessment

The majority of periods rejected by our coarse SQA filter were due to movement artifact when acquiring the CBFV signal (Fig. 2D). After coarse SQA and associated batch selection, the fine SQA (Fig. 2B, E, and F; Supplemental Figure S1) resulted in final data-segment selection for nICP estimation (Fig. 2I) of 10 hours and 9 minutes across 44 study sessions, with a mean uninterrupted segment duration of 4 minutes and 37 seconds.

Waveform Synchronization and Beat-Alignment

The drift between the ABP and CBFV waveforms was approximately 400 msec per 1000 seconds of recording duration (Fig. 3C). The least-squares regression approach to compensate for this waveform drift (de-synchronization) resulted in a zero-mean phase drift between the ABP and CBFV waveforms for each recording (Fig. 3G). The median shift (delay) required to align the ABP and CBFV beat onsets was −66 samples (IQR −89 to −40 samples). The corrections for drift and delay are essential; nICP estimation on the de-synchronized waveforms without these corrections resulted in complete failure of our estimation approach (Fig. 3D), while nICP estimation on synchronized and beat-aligned recordings resulted in physiologically credible results (Fig. 3H).

ABP Correction

The median measured vertical distance, h, between the ICP and ABP transducers across sessions was 11.0 cm (IQR 6.0–21.3 cm). The median hematocrit value was 30.4% (IQR 25.5–33.0%). The calculated median pressure difference thus determined was 8.5 mm Hg (IQR 4.5–16.0 mm Hg).

Estimation Performance

We performed our nICP estimation on windows of 60 consecutive beats from the data segments that were selected by our signal preprocessing pipeline (Fig. 2). Across the 44 studies, the sliding-window approach resulted in 39,480 nICP-to-ICP comparisons, while the hopping-window approach produced 722 such comparisons.

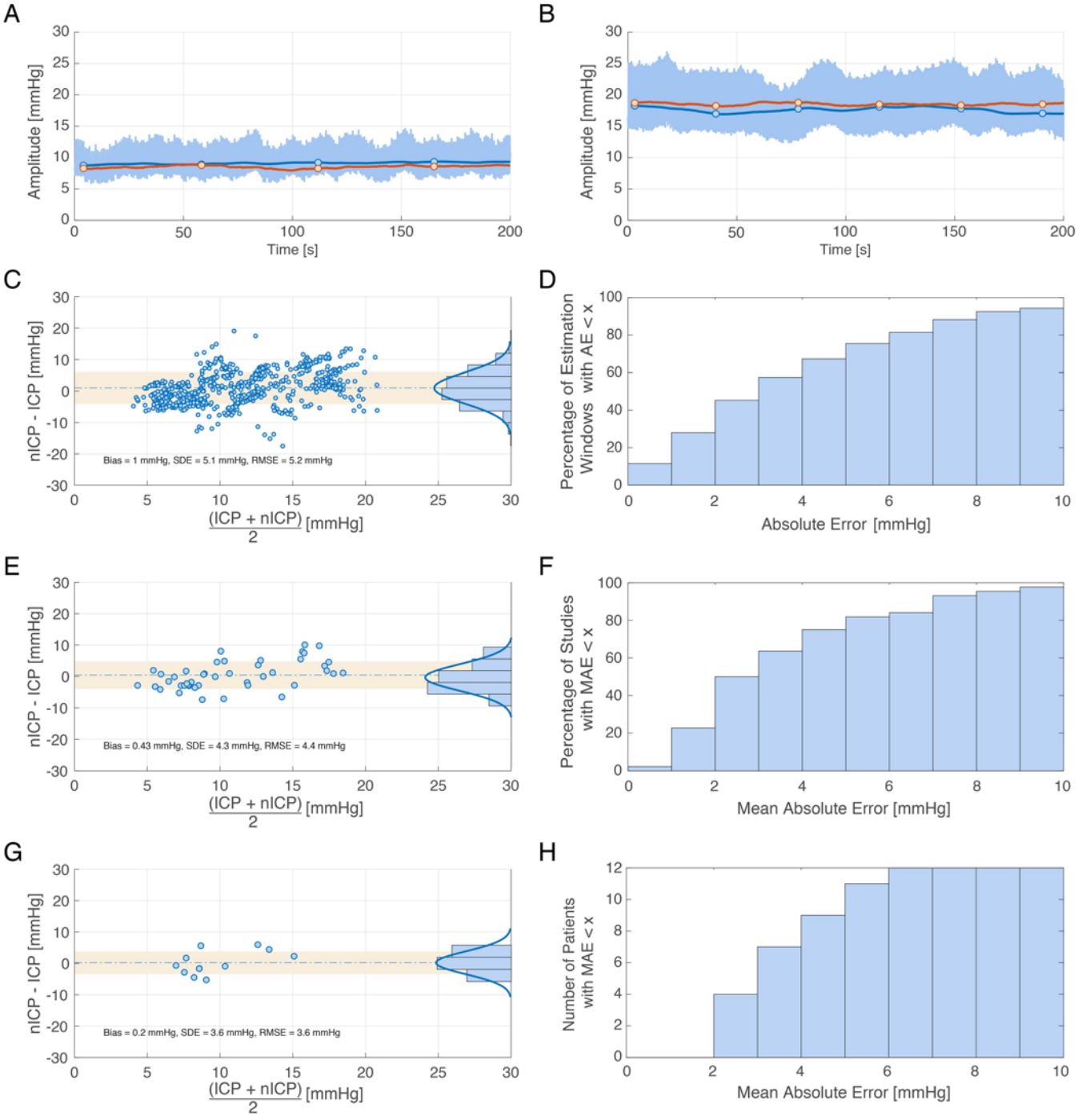

FIG. 4. A and B: ICP waveforms (*light blue*), beat-by-beat mean measured ICP (*dark blue line*), and estimated mean nICP on a sliding (overlapping) window (*red line*) and hopping (nonoverlapping) data windows (*red open circles*) in a patient while ICP is normal (A) and during an episode of elevated ICP (B). **C–H:** Summary statistics and analysis of nICP estimates by Bland-Altman analysis (C, E, and G) and distribution of window-by-window absolute estimation error (D) and mean absolute errors (F and H). C and D: Analysis of 722 hopping window-by-window nICP estimates. E and F: Analysis of 44 study-by-study nICP estimates. G and H: Analysis of 12 patient-by-patient nICP estimates. AE = absolute error.

Figures 4A and 4B show examples of the measured ICP waveform, the beat-by-beat averages of the ICP waveform, and our model-based nICP estimates obtained on sliding (overlapping) and hopping (nonoverlapping) estimation windows during episodes of normal and elevated ICP. In the normal ICP example (Fig. 4A), for the estimation approach using hopping data windows, the bias and SDE are –0.9 mm Hg and 0.5 mm Hg, respectively, with an associated RMSE of 1.0 mm Hg. Likewise, the bias, SDE, and RMSE for the example of elevated ICP (Fig. 4B) are 1.4

TABLE 1. Comparison of nICP estimation results under variations in signal preprocessing

	Estimation Window Approach					
	Sliding	Nonoverlapping				
	Baseline Model	Baseline Model	Nominal Blood Density	w/o HP Correction	w/o Fine SQA	w/o HP Correction & Fine SQA
No. of comparisons	39,480	722	722	722	1286	1286
Bias (mm Hg)	1.05	0.97	0.96	4.10	–0.24	2.93
Median error (mm Hg)	1.01	0.83	0.91	4.35*	–0.35*	3.43*
SDE (mm Hg)	5.10	5.09	5.09	5.56	9.16	9.45
RMSE (mm Hg)	5.20	5.18	5.18	6.91	9.16	9.90
MAE (mm Hg)	4.16	4.15	4.16	5.63	6.24	7.30
MedAE (mm Hg)	3.32	3.32	3.31	4.98	4.05	5.33

HP = hydrostatic pressure.

The first 2 columns summarize the estimation performance using the baseline model with full signal preprocessing pipeline as well as the HP correction of ABP with subject-specific hematocrit values for ρ estimation. The third column summarizes the results when a nominal value of ρ = 1.06 g/ml is used for the blood density. The fourth column shows the estimation results obtained without accounting for the difference in HP between peripheral ABP and MCA ABP. The fifth column summarizes the estimation results if we forgo the fine SQA of the ABP and CBFV waveforms. The final column shows the results if we do not account for HP correction and fine SQA.

* Statistically significant differences in the median estimation error compared with the baseline model ($p < 0.05$).

mm Hg, 1.0 mm Hg, and 1.8 mm Hg, respectively. The sliding-window approach produced essentially the same error statistics.

The overall estimation performance is summarized in Bland-Altman[1] plots (Fig. 4C, E, and G) that display the estimation error (nICP – ICP) against the average of nICP and measured ICP for paired nICP-to-ICP comparisons. For these comparisons, the nICP estimate and the corresponding mean of the measured ICP waveform are computed over the same estimation window. Across all 722 comparisons of the hopping data window approach, we obtained an overall bias of 1.0 mm Hg, SDE of 5.1 mm Hg, and RMSE of 5.2 mm Hg (Fig. 4C). The associated mean absolute error (MAE) and median absolute error (MedAE) are 4.2 mm Hg and 3.3 mm Hg, respectively. When we averaged all nonoverlapping window-by-window nICP estimates for each of the recording sessions, we obtained a bias of 0.4 mm Hg, SDE of 4.3 mm Hg, and RMSE of 4.3 mm Hg across all 44 studies, with MAE and MedAE of 3.5 and 2.9 mm Hg, respectively (Fig. 4E). Averaging all nICP estimates for each patient resulted in a bias of 0.2 mm Hg, SDE of 3.6 mm Hg, and RMSE of 3.6 mm Hg, with MAE and MedAE of 3.1 mm Hg and 2.5 mm Hg, respectively (Fig. 4G). The nICP estimation using the sliding-window approach resulted in essentially the same performance for the window-by-window (Table 1), study-by-study, and patient-by-patient comparisons.

An additional perspective on the performance of our nICP estimation is provided by examining the distribution of the absolute errors for the window-by-window (Fig. 4D) and the MAEs for the study-by-study (Fig. 4F) and patient-by-patient (Fig. 4H) analyses. For the window-by-window and study-by-study estimation approaches, ≥ 80% of all nICP estimates fall within ± 7 mm Hg and ± 6 mm Hg of the reference measurement, respectively. For 9 of 12 subjects, the MAE is 5 mm Hg or less, and all subjects have a MAE of less than 7 mm Hg.

When we performed the hydrostatic pressure correction with a nominal value of 1.06 g/ml for the blood density ρ, the estimation results for hopping and sliding windows remained essentially the same, indicating that the measured variations in hematocrit have negligible effect on the performance of our nICP estimation (Table 1). When we did not apply the hydrostatic pressure correction to the ABP waveform, however, the bias, SDE, and RMSE increased to 4.1 mm Hg, 5.6 mm Hg, and 6.9 mm Hg, respectively, indicating that the hydrostatic pressure correction of the measured ABP waveform is critically important for obtaining clinically meaningful estimation results. Omitting the fine signal quality assessment (step 3 in our signal processing pipeline) to reject beats of poor ABP or CBFV waveform morphology, likewise resulted in unacceptably large errors. Formal statistical analysis of the error distributions associated with each variation in the preprocessing strategy demonstrated that accounting for patient-specific hematocrit did not lead to statistically significantly different results from our baseline model (Table 1). By contrast, foregoing the hydrostatic ABP correction and/or fine SQA significantly increased the error, demonstrating that these steps are essential (Table 1).

We also explored whether the algorithm could correctly classify elevated ICP, defined here as mean measured ICP > 15 mm Hg (approximately 20 cm H_2O). When using an estimated nICP of 15 mm Hg as a threshold for classification, we obtained a sensitivity of 74% and specificity of 77% for detection of elevated ICP. By varying the nICP threshold from 0 mm Hg to 30 mm Hg, we obtained the full ROC curve, with the definition of elevated ICP being mean measured ICP > 15 mm Hg. Performing this analysis on all 722 nonoverlapping nICP-to-ICP comparisons, we obtained an AUC of 0.79 (Fig. 5). When we performed the same analysis on the study-by-study averaged estimation results, we obtained an AUC of 0.83, and a sensitivity of 71% and a specificity of 86% for the nICP threshold of 15 mm Hg. The study-by-study sensitivity and specificity resulted in a positive likelihood ratio value of 5.1, suggest-

ing a moderate posttest increase in the probability of elevated ICP if nICP is > 15 mm Hg.[7] Likewise, the negative likelihood ratio value is 0.33, suggesting a moderate posttest decrease in the probability of elevated ICP if nICP < 15 mm Hg.

Finally, we assessed the risk of misclassifying patients on the basis of the nICP estimates. To do this, we computed the (empirical) probability of observing a measured mean ICP > 15 mm Hg, given that the corresponding nICP estimate is < 10 mm Hg. For the hopping-window approach, that probability was 2.4% in our data set. Likewise, the (empirical) probability of observing a mean measured ICP < 10 mm Hg, given that the corresponding nICP estimate is > 15 mm Hg is 13.2%. Thus, the overall chance of missing a patient with elevated ICP is only 2.4% if the nICP estimates suggest a normal ICP level, while there is a mildly greater (13.2%) chance of having falsely declared an elevated ICP if the underlying ICP is actually normal.

Real-Time nICP Computation

The signal quality assessment and time-alignment pipeline presented here along with all computations necessary for nICP estimation were implemented in MATLAB (MathWorks). Execution of all computational steps for a 60-beat estimation window took 11 msec on a standard Intel Core i7 processor with 16 GB of RAM. This demonstrates that the preprocessing and estimation computations can be performed well within a fraction of a cardiac cycle duration. Thus, even the sliding-window estimation approach in which ICP estimates are updated every beat can be executed in real time.

Discussion

Physicians know how to manage patients with obvious clinical signs of elevated ICP, usually when the level is greater than 25 mm Hg. In contrast, they do not have clinical signs to guide treatment when the level is in the abnormal range of 15 to 25 mm Hg. Under such circumstances, one approach that is used in adults in the emergency department is to measure optic nerve sheath diameter, which gives some indication of whether ICP is elevated or not.[16] This methodology is not suitable for continuous monitoring and does not provide an absolute ICP value. In addition, this technique is not patient specific, as the ultrasound measurements need to be interpreted with reference to established population-derived norms. Patient-specific ICP determination would be a key advancement for the care of children with atypical development (e.g., craniosynostosis, myelomeningocele, genetic syndromes, cardiac defects/malformations) for whom population-derived norms are of questionable relevance and reliability. Such "atypical" patients comprise the majority of pediatric patients for whom personalized ICP assessment is most needed, apart from the aforementioned patients with acute TBI or encephalopathy. Our work here has made 2 key contributions toward realizing such noninvasive personalized nICP assessment, using a model-based signal processing approach.

First, we developed a fully automated pipeline for signal quality assessment, waveform synchronization and alignment, and nICP estimation that can work in real time. The TCD-based CBFV waveform recordings are prone to waveform artifacts, noise, and signal dropouts, particularly in noncooperative patients. Previous approaches to model-based nICP estimation have relied on visual inspection of data records and manual selection of data segments to ensure that waveform segments are of sufficiently high signal quality to pass them to the estimation algorithm.[9,13] The signal preprocessing approach described here also overcomes a major issue in multimodal waveform analyses from multiple bedside devices—their lack of time synchronization which leads to drift. Our approach can work after data collection has occurred, and it is therefore applicable to a broader set of biomedical engineering applications where waveforms are collected from different bedside monitoring devices.

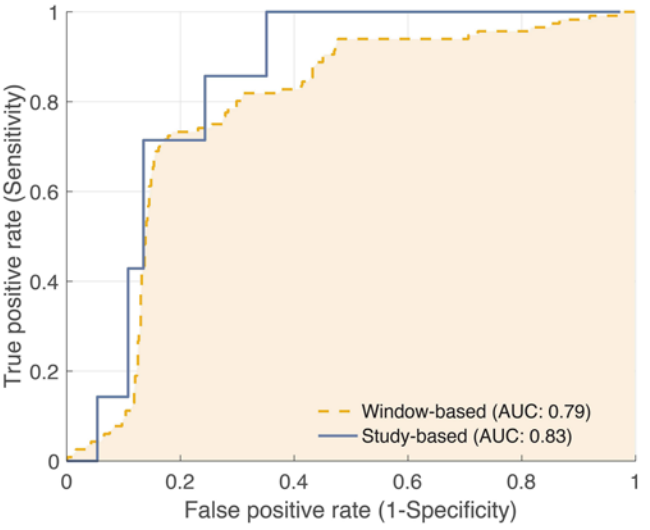

FIG. 5. ROC curves for detection of intracranial hypertension, defined as mean measured ICP > 15 mm Hg (approximately 20 cm H_2O). Window-by-window analysis of the hopping (nonoverlapping) estimation window approach resulted in 722 60-beat estimation windows and an AUC of 0.79. Averaging the window-by-window nICP estimates for each study resulted in an AUC of 0.83 across all 44 studies.

Second, we demonstrated that our approach was of sufficient robustness that it performed well across the full pediatric age range (and therefore body and vascular system sizes) and across various etiologies of coma. We also demonstrated that it is sufficiently accurate and precise for clinical decision-making. A recent meta-analysis comparing the accuracy of invasive ICP monitoring approaches showed a pooled mean difference between paired readings of 2 invasive probes of 1.5 mm Hg (95% CI 0.7–2.3 mm Hg).[22] In those studies included in the meta-analysis with 10 or more subjects, the reported SDEs ranged from 1.1 mm Hg to 7.8 mm Hg. Our model-based nICP estimation produced a bias of about 1.0 mm Hg and associated SDE of 5.1 mm Hg, which matches the clinically accepted accuracy and range of precision errors for routinely used invasive ICP monitors. Additionally, the approach yields a moderate posttest increase in the detection of elevated ICP, defined here as mean measured ICP > 15 mm Hg, which can help with triage decisions.

The current system is designed to permit real-time and continuous monitoring by an estimate of nICP based on measurements of radial ABP and TCD-based MCA CBFV. In our experience, high-quality MCA CBFV measurements can be obtained reliably with minimal training. While the intra- and interoperator reliability of TCD-based velocimetry measurements are generally considered good,[5,12,19] we limited the risk of variation by having 2 trained members of the study staff conduct essentially all TCD measurements. Furthermore, our model-based nICP estimates are comparatively insensitive to (constant) scaling of the CBFV waveform as would be encountered if the same vessel were insonated under different (but constant) Doppler angles.[9] We envisage that future iterations of our approach incorporate noninvasive ABP and operator-independent CBFV recording systems to enable continuous nICP estimation.[15,17,18]

We note some insights and limitations arising from the work presented here. Most importantly, careful bedside data collection with measurement of ABP and CBFV transducer heights for hydrostatic pressure correction is required, as is the need for careful signal quality assessment. One issue is that we observed only a limited range in ICP per patient and across patients, with few measurements > 20 mm Hg. Expansion of the patient pool will allow us to expand the ICP range and also to determine whether our approach can detect gradients in measured ICP in unilateral injuries.

Conclusions

We developed a fully automated approach to noninvasive, patient-specific, and calibration-free ICP monitoring based on analysis of simultaneous waveform recordings of ABP and MCA CBFV from bedside TCD ultrasonography. Our results demonstrate a promising route toward safe, robust, and continuous nICP estimation at clinically acceptable accuracy and precision errors. This technique performed robustly in the ICP range of 15 to 25 mm Hg. This is a level at which management after severe TBI in children has been deemed necessary in a variety of pediatric protocols, yet for which noninvasive and patient-specific technologies are currently still lacking.[10] We believe that this technology could transform surveillance and interventions beyond the care of pediatric patients with moderate to severe TBI to a number of coma-inducing conditions complicated by intracranial hypertension, worldwide, such as central nervous system infection.[14]

Acknowledgments

This study was supported, in part, by the National Institute of Neurological Disorders and Stroke (Grant R21 NS084264); Maxim Integrated Products; and from a Neurocritical Care Chair Award from the Department of Anesthesiology, Critical Care, and Pain Medicine at Boston Children's Hospital.

References

1. Altman DG, Bland JM: Comparison of methods of measuring blood pressure. **J Epidemiol Community Health 40:**274–277, 1986
2. Bennett TD, DeWitt PE, Greene TH, Srivastava R, Riva-Cambrin J, Nance ML, et al: Functional outcome after intracranial pressure monitoring for children with severe traumatic brain injury. **JAMA Pediatr 171:**965–971, 2017
3. Chesnut RM, Temkin N, Carney N, Dikmen S, Rondina C, Videtta W, et al: A trial of intracranial-pressure monitoring in traumatic brain injury. **N Engl J Med 367:**2471–2481, 2012
4. Constant I, Laude D, Elghozi JL, Murat I: Assessment of short-term blood pressure variability in anesthetized children: a comparative study between intraarterial and finger blood pressure. **J Clin Monit Comput 15:**205–214, 1999
5. Demolis P, Chalon S, Giudicelli JF: Repeatability of transcranial Doppler measurements of arterial blood flow velocities in healthy subjects. **Clin Sci (Lond) 84:**599–604, 1993
6. Fanelli A, Heldt T: Signal quality quantification and waveform reconstruction of arterial blood pressure recordings. **Conf Proc IEEE Eng Med Biol Soc 2014:**2233–2236, 2014
7. Grimes DA, Schulz KF: Refining clinical diagnosis with likelihood ratios. **Lancet 365:**1500–1505, 2005
8. Hinghofer-Szalkay H, Kenner T, Leopold H, Holzer H: [Application of the mechanical oscillator technique for the measurement of blood density and hematocrit (author's transl).] **Klin Wochenschr 57:**1163–1167, 1979 (German)
9. Kashif FM, Verghese GC, Novak V, Czosnyka M, Heldt T: Model-based noninvasive estimation of intracranial pressure from cerebral blood flow velocity and arterial pressure. **Sci Transl Med 4:**129ra44, 2012
10. Kochanek PM, Tasker RC, Bell MJ, Adelson PD, Carney N, Vavilala MS, et al: Management of pediatric severe traumatic brain injury: 2019 consensus and guidelines-based algorithm for first and second tier therapies. **Pediatr Crit Care Med 20:**269–279, 2019
11. Kochanek PM, Tasker RC, Carney N, Totten AM, Adelson PD, Selden NR, et al: Guidelines for the Management of Pediatric Severe Traumatic Brain Injury, Third Edition: Update of the Brain Trauma Foundation Guidelines. **Pediatr Crit Care Med 20 (3S Suppl 1):**S1–S82, 2019
12. Maeda H, Etani H, Handa N, Tagaya M, Oku N, Kim BH, et al: A validation study on the reproducibility of transcranial Doppler velocimetry. **Ultrasound Med Biol 16:**9–14, 1990
13. Noraky J, Verghese GC, Searls DE, Lioutas VA, Sonni S, Thomas A, et al: Noninvasive intracranial pressure determination in patients with subarachnoid hemorrhage. **Acta Neurochir Suppl 122:**65–68, 2016
14. Odetola FO, Clark SJ, Lamarand KE, Davis MM, Garton HJ: Intracranial pressure monitoring in childhood meningitis with coma: a national survey of neurosurgeons in the United States. **Pediatr Crit Care Med 12:**e350–e356, 2011
15. Pietrangelo SJ, Lee HS, Sodini CG: A wearable transcranial Doppler ultrasound phased array system. **Acta Neurochir Suppl 126:**111–114, 2018
16. Robba C, Santori G, Czosnyka M, Corradi F, Bragazzi N, Padayachy L, et al: Optic nerve sheath diameter measured sonographically as non-invasive estimator of intracranial pressure: a systematic review and meta-analysis. **Intensive Care Med 44:**1284–1294, 2018
17. Seo J, Pietrangelo SJ, Sodini CG, Lee HS: Motion tolerant unfocused imaging of physiological waveforms for blood pressure waveform estimation using ultrasound. **IEEE Trans Ultrason Ferroelectr Freq Control 65:**766–779, 2018
18. Seo J, Sodini CG, Lee HS: Monitoring of pulse pressure and arterial pressure waveform changes during the Valsalva maneuver by a portable ultrasound system. **Conf Proc IEEE Eng Med Biol Soc 2018:**3817–3820, 2018
19. Totaro R, Marini C, Cannarsa C, Prencipe M: Reproducibility of transcranial Doppler sonography: a validation study. **Ultrasound Med Biol 18:**173–177, 1992
20. van Belle G, Fisher LD, Heagerty PJ, Lumley T: **Biostatis-**

tics—A Methodology for the Health Sciences, ed 2. Hoboken, NJ: John Wiley & Sons, 2004
21. Wadehn F, Fanelli A, Heldt T: Segmentation of TCD cerebral blood flow velocity recordings. **arXiv:**1806.09994, 2018
22. Zacchetti L, Magnoni S, Di Corte F, Zanier ER, Stocchetti N: Accuracy of intracranial pressure monitoring: systematic review and meta-analysis. **Crit Care 19:**420, 2015
23. Zong W, Heldt T, Moody GB, Mark RG: An open-source algorithm to detect onset of arterial blood pressure pulses. **Comput Cardiol 30:**259–262, 2003

Disclosures

The Massachusetts Institute of Technology has received patent protection of the core estimation algorithm, listing T.H. as one of the inventors.

Author Contributions

Conception and design: Heldt, Robinson, Tasker. Acquisition of data: all authors. Analysis and interpretation of data: Heldt, Fanelli, Vonberg, Smith, Robinson, Tasker. Drafting the article: Heldt, Fanelli, Tasker. Critically revising the article: all authors. Reviewed submitted version of manuscript: all authors. Approved the final version of the manuscript on behalf of all authors: Heldt. Statistical analysis: Heldt, Fanelli. Study supervision: Heldt, Robinson, Tasker.

Supplemental Information

Online-Only Content

Supplemental material is available with the online version of the article.

Supplementary Material. https://thejns.org/doi/suppl/10.3171/2019.5.PEDS19178.

Correspondence

Thomas Heldt: Institute for Medical Engineering & Science, Massachusetts Institute of Technology, Cambridge, MA. thomas@mit.edu.

Supplementary Materials

Fully automated, real-time, calibration-free, continuous noninvasive estimation of intracranial pressure in children

Andrea Fanelli, PH.D.,[1] Frederick W. Vonberg, M.B., B.S.,[1,2] Kerri L. LaRovere, M.D.,[3] Brian Walsh, PH.D.,[2] Edward R. Smith, M.D.,[4] Shenandoah Robinson, M.D.,[4,5] Robert C. Tasker, M.B., B.S., M.D.,[2,3] Thomas Heldt, PH.D.[1]

[1]Institute for Medical Engineering and Science, Massachusetts Institute of Technology, Cambridge, Massachusetts; [2]Department of Anesthesiology, Critical Care and Pain Medicine, Boston Children's Hospital, Boston, Massachusetts; [3]Department of Neurology, Boston Children's Hospital, Boston, Massachusetts; [4]Department of Neurosurgery, Boston Children's Hospital, Boston, Massachusetts; and [5]Department of Neurosurgery, Johns Hopkins University, Baltimore, Maryland.

Mathematical Formulation of Estimation Problem

As described in Kashif *et al.*[1], the circuit model representation shown in Figure 1a of the relevant cerebrovascular physiology is mathematically described by the first-order differential equation

$$CBFV(t) = \frac{ABP(t)-ICP}{R} + C\frac{d}{dt}\left[ABP(t) - ICP\right] \qquad (1)$$

where $CBFV(t)$ is the cerebral blood flow velocity waveform at the middle cerebral artery (MCA); $ABP(t)$ is the corresponding arterial blood pressure waveform; *C* is the lumped cerebrovascular and brain tissue compliance; *R* is the resistance to blood flow through the MCA territory, and ICP is the intracranial pressure. Equation (1) imposes a mathematical constraint between the model parameters *R, C*, and *ICP* on the one hand and the measurable waveforms $CBFV(t)$ and $ABP(t)$ the other hand. To estimate nICP, we record the MCA CBFV and the radial ABP waveforms and solve Equation (1) to obtain estimates of *R, C*, and *ICP*. Rather than solving Equation (1) for each cardiac cycle, we assume that *R*, *C*, and *ICP* are constant for the duration of 60 beats (estimation window) and estimate one value for *R*, *C*, and *ICP* for each 60-beat estimation window.

To arrive at an nICP estimate, we decompose the estimation problem by first estimating *C* during the early ejection period when the rate of change in ABP is largest and flow into the MCA territory is predominantly stored in the expansion of the elastic arteries. Assuming the flow through the resistance is negligible during the ejection period, Equation (1) can be approximated as

$$\left[ABP(t_1) - ABP(t_2)\right] \cdot C \approx \int_{t_1}^{t_2} CBFV(t')dt' \qquad (2)$$

where t_1 and t_2 are the onset and end of the sharp systolic upslope in the ABP wavelet. Equation (2) can be formulated for each beat in the estimation window, and the resultant set of equations can then be solved in a least-square manner to arrive at the compliance estimate $\hat{C}$. With $\hat{C}$ so estimated, the flow $CBFV_R(t)$ through the resistive element can be approximated as

$$CBFV_R(t) = CBFV(t) - \hat{C} \cdot \frac{d}{dt}APB(t) \qquad (3)$$

Making use of the constitutive relation for flow through the resistive element, ICP was expressed as

$$ICP = ABP(t) - R \cdot CBFV_R(t) \qquad (4)$$

and under the assumption of constant ICP over a beat and estimation window, the resistance R can be estimated by evaluating Equation (4) at two (or more) time points during a cardiac cycle and eliminating the constant ICP:

$$[CBFV_R(t_2) - CBFV_R(t_1)] \cdot \hat{R} = ABP(t_2) - ABP(t_1) \qquad (5)$$

The final estimate of ICP is then determined according to

$$\widehat{ICP} = \overline{ABP} - \hat{R} \cdot \overline{CBFV_R} \qquad (6)$$

where the overbars indicate beat-averaged values of ABP and $CBFV_R$. Equations (5) and (6) are likewise evaluated for each beat in the 60-beat estimation window and solved in a least-square manner to arrive at one estimate $\hat{R}$ and $\widehat{ICP}$ for each estimation window.

Fine Signal Quality Assessment

We evaluated the beat-by-beat ABP waveform quality by first computing, for each beat, the mean absolute sample-by-sample difference $d_i = \underset{j\in[n(i),\ n(i+1)-1]}{\text{mean}} \|ABP(j) - ABP(j+1)\|$, where $n(i)$ denotes the onset sample of the i-th beat, and the interval $[n(i),\ n(i+1)-1]$ spans all samples of the i-th beat. We computed a standardized score $\widehat{d_i} = \frac{\|d_i - \overline{d_i}\|}{\overline{d_i}}$ by subtracting and normalizing d_i by a running average of the past 20 mean absolute deviations $\overline{d_i} = \frac{1}{20}(d_{i-1} + d_{i-2} + \cdots + d_{i-20})$. This beat-by-beat, normalized, absolute deviation metric $\widehat{d_i}$ assumes large values in regions in which the waveform morphology is corrupted by noise and artifact. We chose an empirical threshold of 0.3 to identify beats of questionable signal quality and to binarize the beat-by-beat ABP signal quality metric (Supplemental Figure S1).

The beat-by-beat fine CBFV signal quality was determined by first computing the spectral correlation between the ABP and CBFV signals over a sliding window of 8 s in duration and then quantifying the deviation

of each CBFV wavelet from an adaptively updated wavelet template.[2] Since the lower frequency components of the ABP and CBFV waveforms are dominated by the cardiac beating frequency and its harmonics, the power spectra of the two signals normally have dominant peaks at the same frequencies. During periods of significant noise and artifact in one of the signals, the strength of this spectral correlation declines. In a first step, regions of the CBFV signal were identified for rejection if – in the frequency range from 0.5 to 5.0 Hz – the correlation coefficient between the power spectral densities of the CBFV and ABP was below the empirical threshold of 0.5. Subsequently, a CBFV wavelet template was obtained on potentially acceptable beats by computing the median CBFV wavelet across all beats that had not been rejected. This template was then used to assess the quality of the CBFV waveform on a beat-by-beat basis and to identify beats that had a large normalized mean-squared error when referenced to the template.

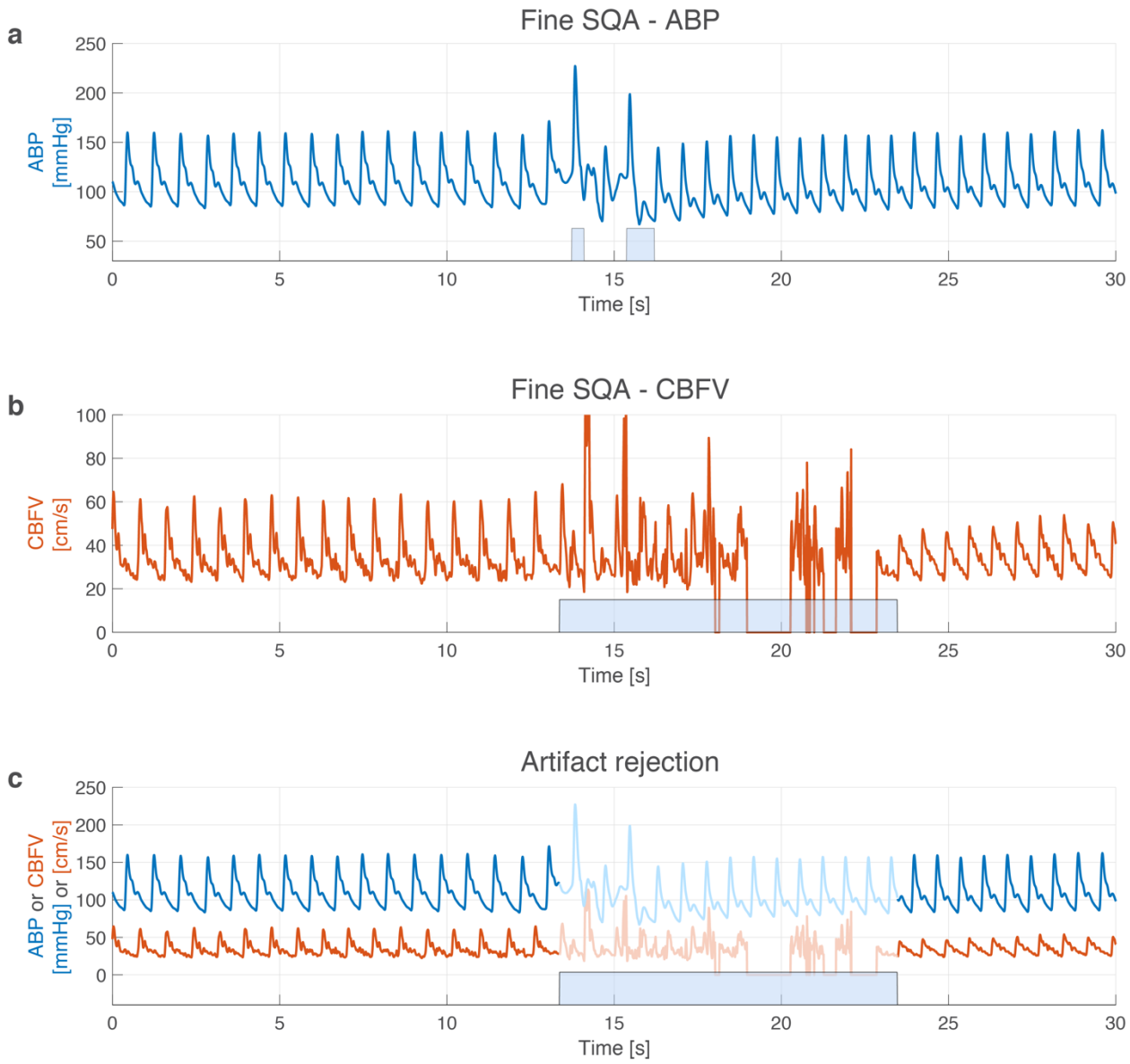

Supplemental Figure S1 Fine Signal-Quality Assessment (SQA). Examples of applying our fine SQA filter to (**a**) the ABP and (**b**) the CBFV waveform. Regions of poor waveform morphology are flagged (marked here in blue). (**c**) Regions of the input data are flagged and excluded from further analysis if either the ABP or the CBFV fine SQA flags indicate poor waveform quality.

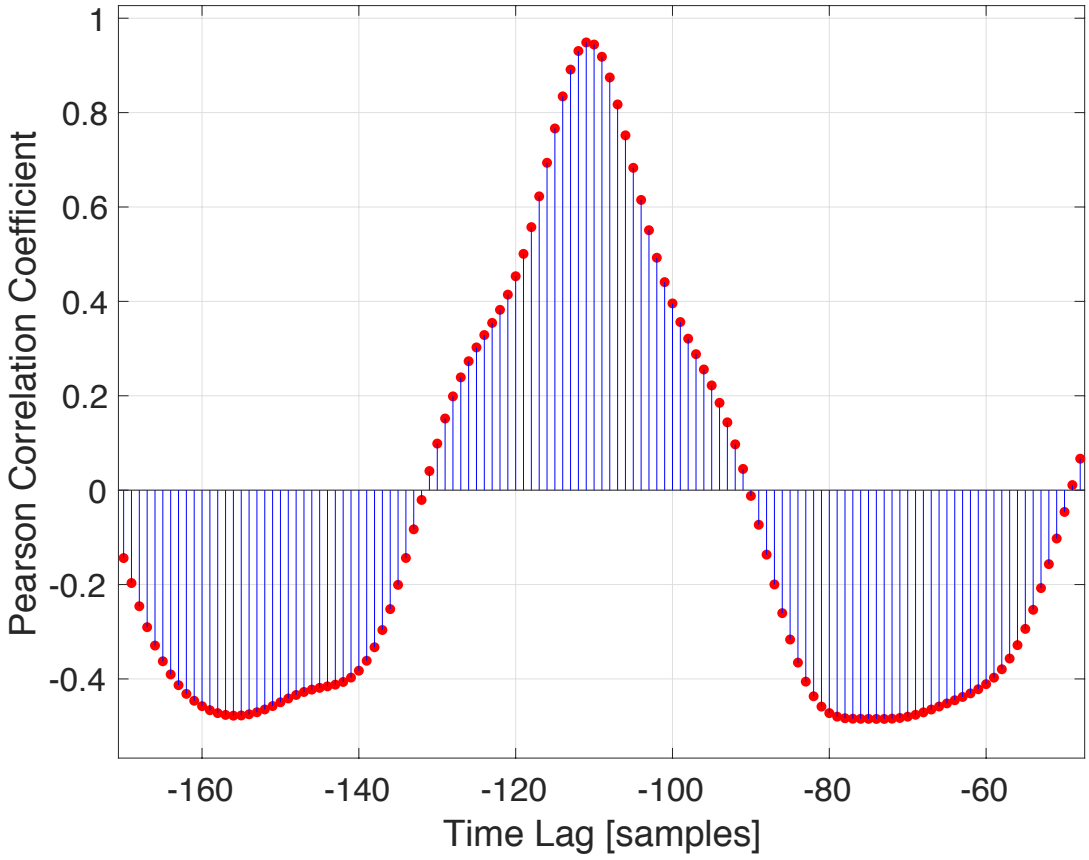

Supplemental Figure S2 Beat-onset alignment. Sample cross-correlation between the ABP and CBFV waveforms. The time lag associated with the peak of the cross-correlation identifies the starting delay between the waveforms. We correct for this delay by subtracting it from the CBFV time stamps to achieve alignment of corresponding ABP and CBFV wavelets.

1. Kashif FM, Verghese GC, Novak V, Czosnyka M, Heldt T: Model-based noninvasive estimation of intracranial pressure from cerebral blood flow velocity and arterial pressure. **Sci Transl Med 4:**129ra144, 2012
2. Wadehn F, Fanelli A, Heldt T: Segmentation of TCD Cerebral Blood Flow Velocity Recordings, in: arxiv.org, 2018, Vol 2018